PNAS
www.pnas.org

Supplementary Information for

The 2020 COVID-19 pandemic and atmospheric composition: back to the future

Joshua L. Laughner, Jessica L. Neu, David Schimel, Paul O. Wennberg, et al.

Full author list:
Joshua L. Laughner, Jessica L. Neu, David Schimel, Paul O. Wennberg, Kelley Barsanti, Kevin Bowman, Abhishek Chatterjee, Bart Croes, Helen Fitzmaurice, Daven Henze, Jinsol Kim, Eric A. Kort, Zhu Liu, Kazuyuki Miyazaki, Alexander J. Turner, Susan Anenberg, Jeremy Avise, Hansen Cao, David Crisp, Joost de Gouw, Annmarie Eldering, John Fyfe, Dan Goldberg, Kevin R. Gurney, Sina Hasheminassab, Francesca Hopkins, Cesunica E. Ivey, Dylan B.A. Jones, Nicole S. Lovenduski, Randall V. Martin, Galen A. McKinley, Lesley Ott, Benjamin Poulter, Muye Ru, Stanley P. Sander, Neil Swart, Yuk L. Yung, Zhao-Cheng Zeng, and the rest of the Keck Institute for Space Studies "COVID-19: Identifying Unique Opportunities for Earth System Science" study team

Corresponding Authors:
Joshua L. Laughner: jlaugh@caltech.edu
Jessica L. Neu: jessica.l.neu@jpl.nasa.gov
David Schimel: david.schimel@jpl.nasa.gov, or
Paul O. Wennberg: wennberg@gps.caltech.edu

This PDF file includes:

Additional figures

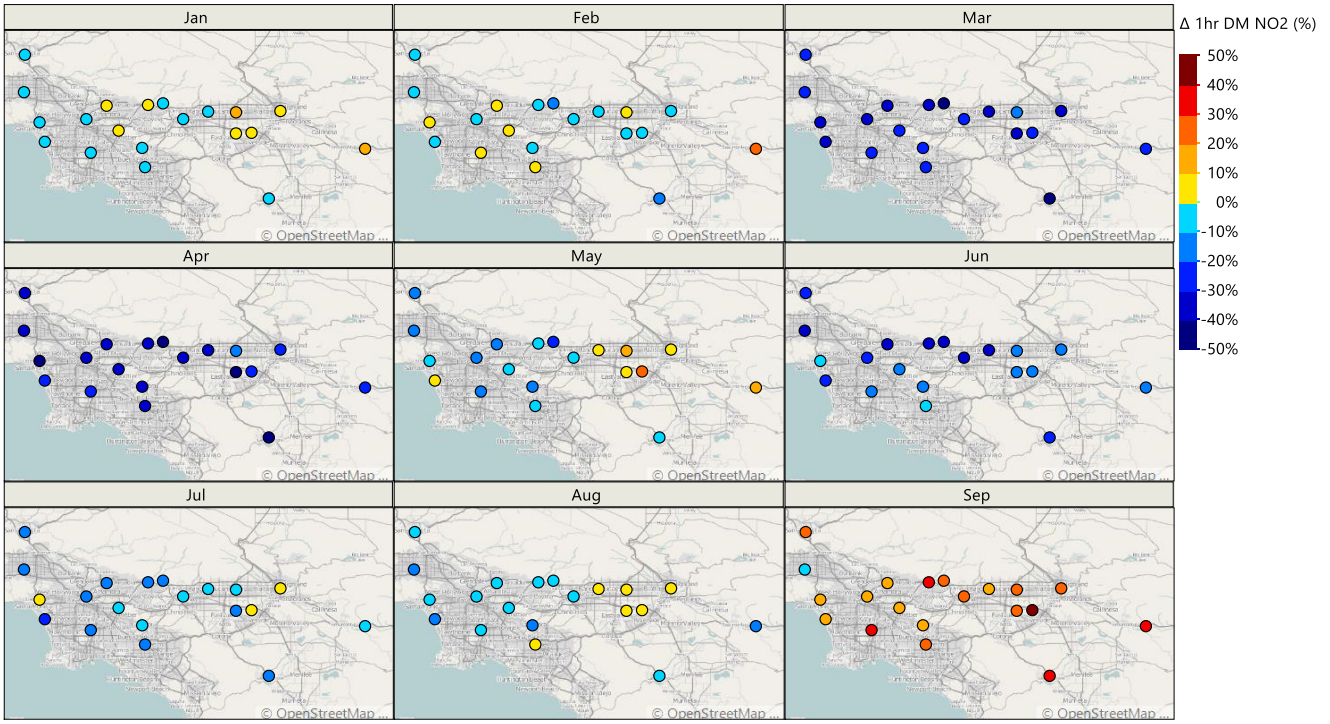

Fig. S1. Change in 1 hr daily maximum (DM) NO_2 in 2020 relative to the average of 2015 to 2019 at the California Air Resources Board sites throughout the South Coast Air Basin.

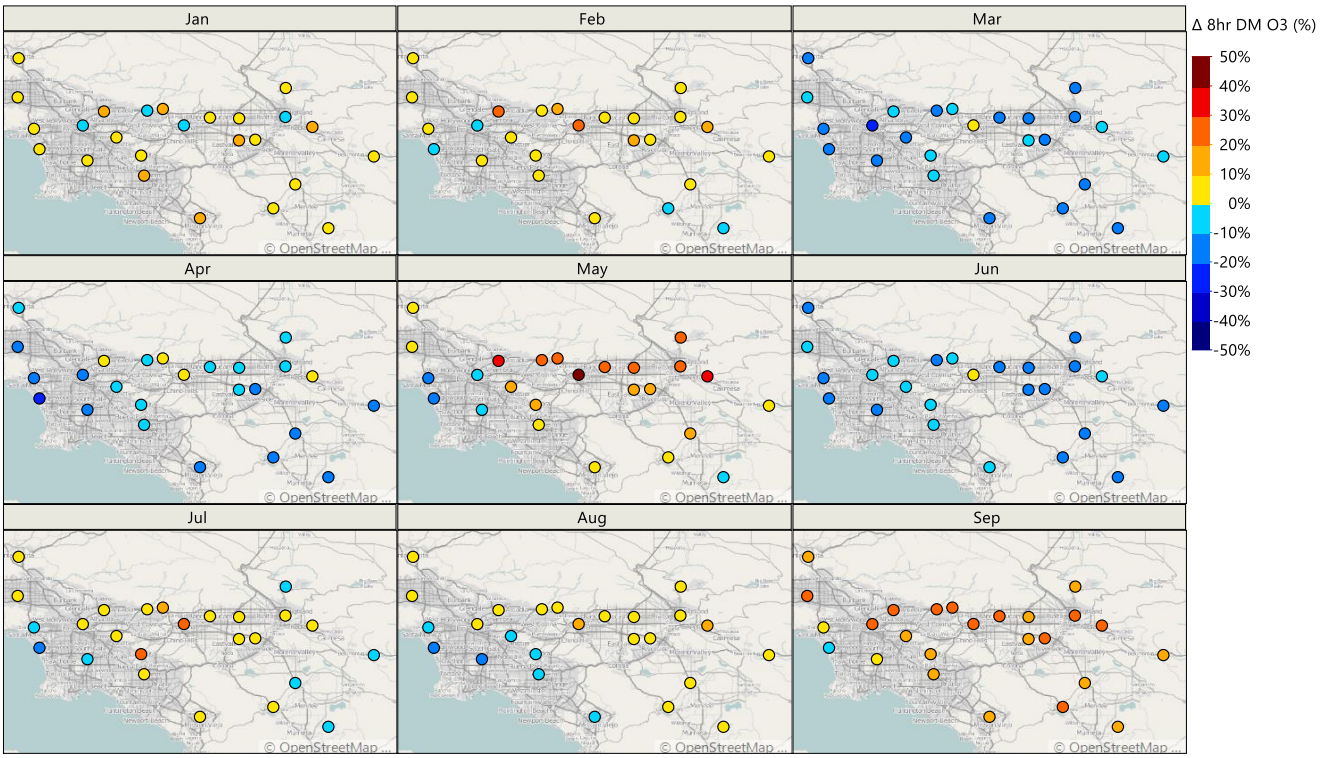

Fig. S2. Change in 8 hr daily maximum (DM) O_3 in 2020 relative to the average of 2015 to 2019 at the California Air Resources Board sites throughout the South Coast Air Basin.

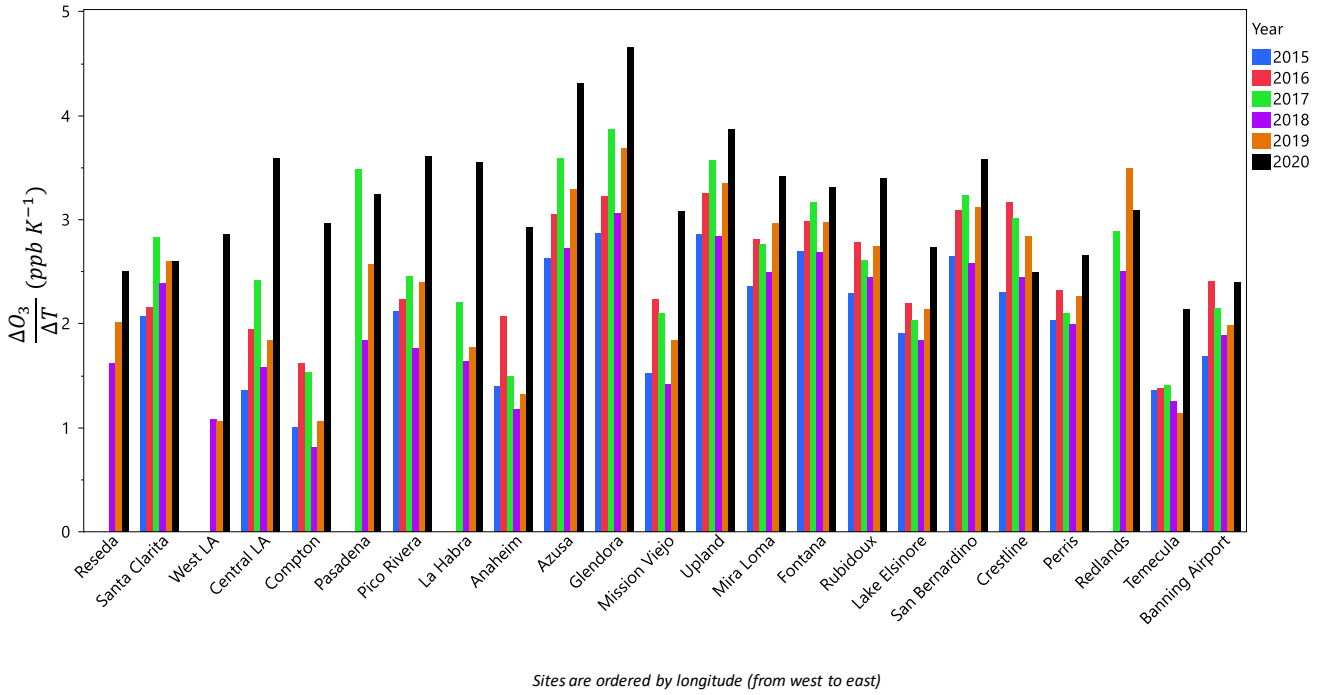

Fig. S3. Average derivatives of O_3 response vs. temperature between May and September at California Air Resources Board sites throughout the South Cost Air Basin for years 2015–2020. Each group of bars is one site, and are ordered by longitude (west to east).

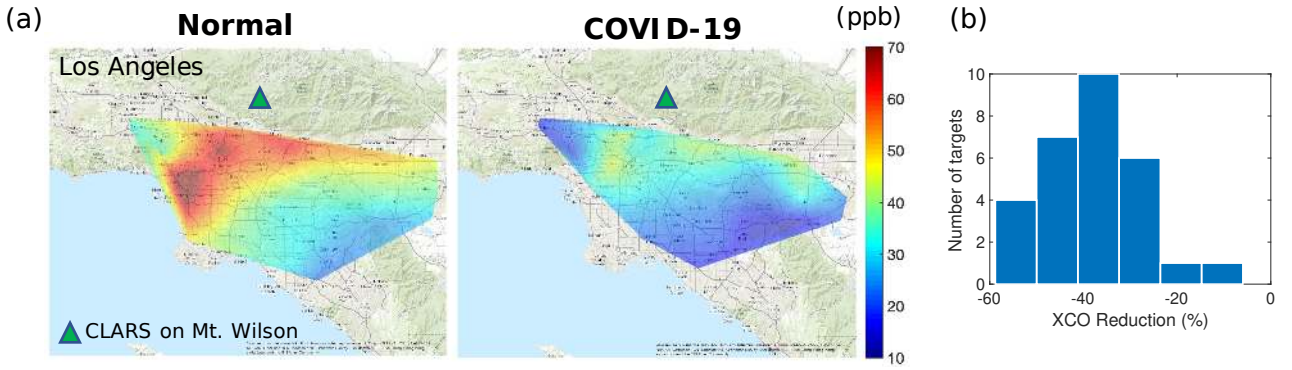

Fig. S4. (a) Maps of CO column abundance (XCO) in excess of the background in the Los Angeles (LA) basin averaged for the month of April. Left panel (Normal): April noontime average for 2012-2019. Right panel (COVID-19): April 2020 during lockdown. These maps are interpolated from the 33 surface observation targets by CLARS-FTS; **(b)** The histogram of difference between XCO excess measurements in (a) for all the surface observation targets. The averaged XCO excess reduction is 37.5% on average due to the lockdown order.

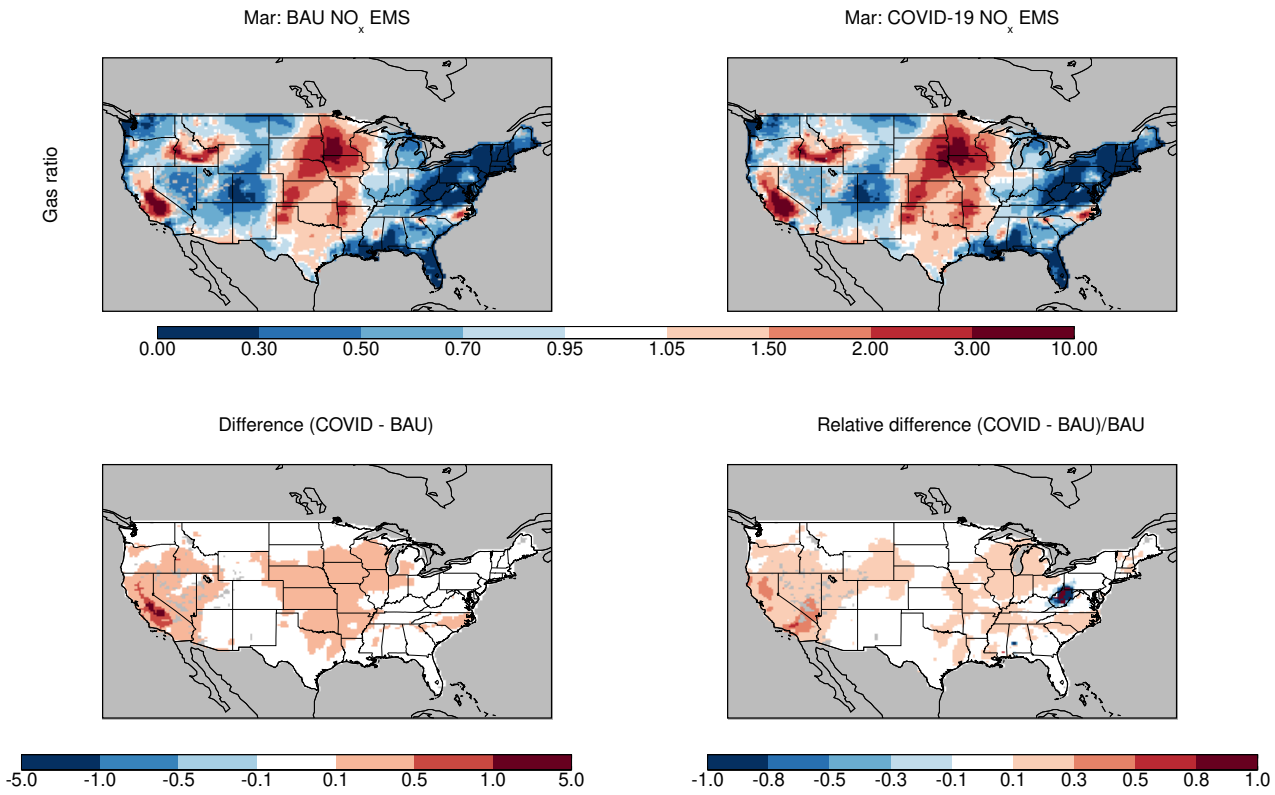

Fig. S5. Average change in gas ratios for March 2020 between a model simulation using business as usual (BAU) NO_x emissions and one using emissions based on NO_2 observations for March 2020 (COVID-19). The gas ratio is described in $\mathrm{Eq.}\ (1)$; a value < 1 indicates NH_3 limited nitrate aerosol formation; a value > 1 indicates NO_x limited aerosol formation.

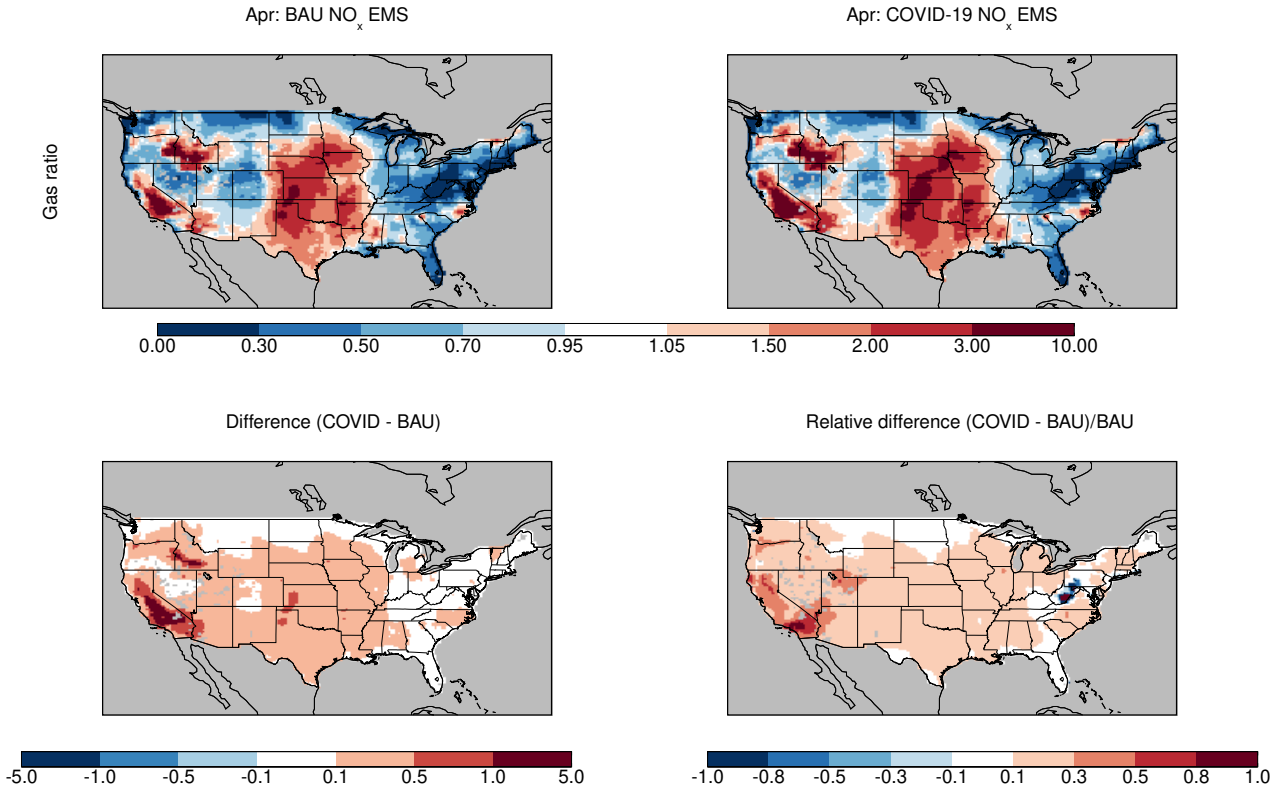

Fig. S6. Same as Fig. S7, but for April 2020.

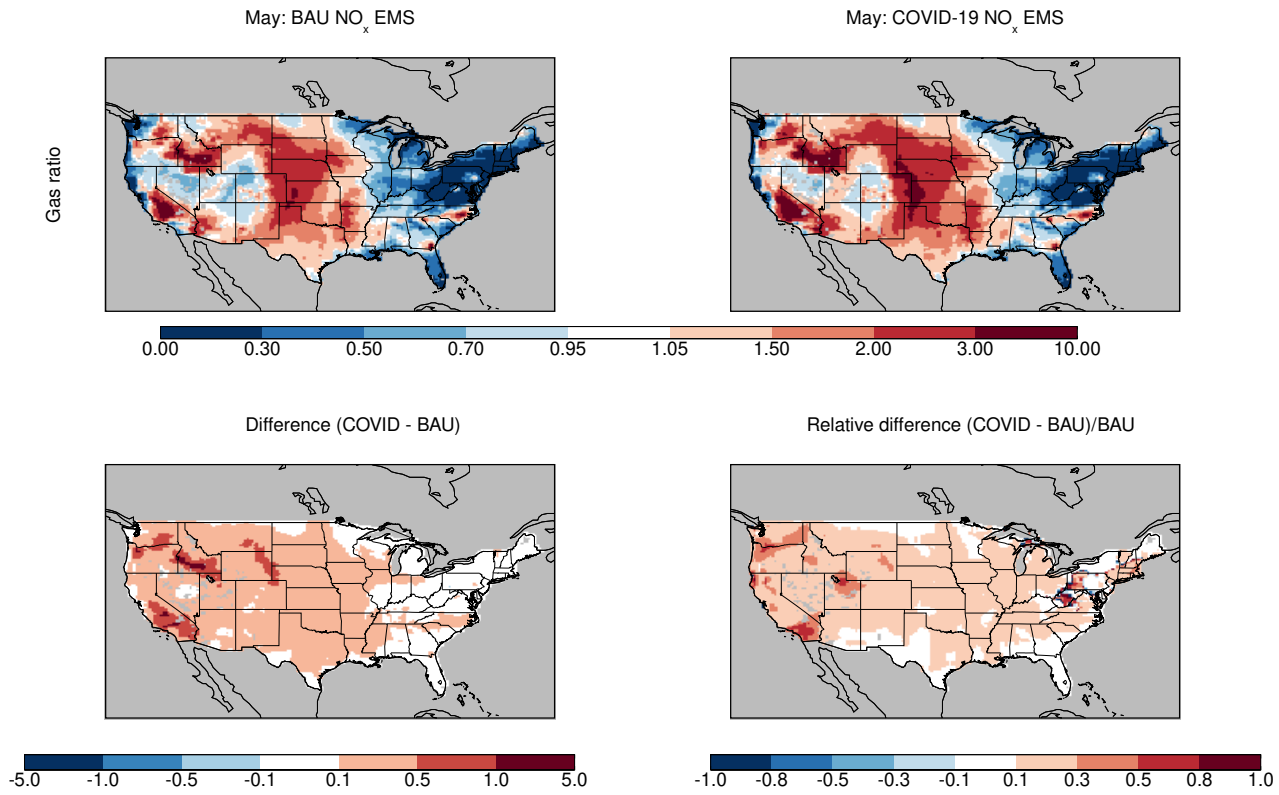

Fig. S7. Same as Fig. S7, but for May 2020.

Supporting Information Text

Methods

Public data. All public datasets used in this study are shown in Table S1.

Equivalent Emissions Year Calculations. For the CO_2 emissions in Fig.2a, we used 2005-2018 fossil fuel emissions from the Global Carbon Budget 2019 (12). For 2019, we assumed a +0.1% increase from 2018 based on Supplementary Data in Le Quere et al (13). For 2020 we used a 7% decrease from the 2019 value with a ± 1% uncertainty, based on Le Quere et al (13) and Liu et al (14). The 2020 emissions are 9.29 (± 0.10) GtC/yr; this corresponds to somewhere between 2010 (9.05 GtC/yr) and 2012 (9.50 GtC/yr). For CH_4, we use the anthropogenic emissions based on the EDGARv4.3.2 and GFED4.1s emissions inventories as published in the Global Methane Budget 2000-2017 (15). The emissions trajectory beyond 2017 is for illustrative purposes only and is not based on any data. For the global NO_x emission trajectory in Fig. 2 we used 2005-2020 emissions from the assimilation system described in the subsection "Global ozone production efficiency calculation" below. The equivalent year of 1999 ± 3.5 years was determined by applying the percent reduction between the average emissions over 2010-2014 and the 2020 emissions as determined by the assimilation system (-15.8%) to the 2010-2014 emissions from the CEDS and EDGAR5.0 inventories.

For Fig 2b, we again used the NO_x emissions from the assimilation system. For countries whose emissions have been monotonically increasing since 2005, we calculate the prior year with the same emissions as 2020. For countries whose emissions decreased over all or part of the 2005-2019 period, we use the 2015-2019 rate of decline to project emissions into the future.

Human activity metrics. The human activity metrics in Fig. 3 include the Oxford Coronavirus Government Response Index (1), Opensky-derived flight data (2, 16, 17), Port of LA container moves (https://www.portoflosangeles.org/business/statistics/container-statistics, last accessed 30 Oct 2020), Port of Oakland container moves (https://www.oaklandseaport.com/performance/facts-figures/, last accessed 30 Oct 2020), Caltrans PeMS daily vehicle counts (http://pems.dot.ca.gov/, last accessed 28 Oct 2020), Apple driving mobility data (https://covid19.apple.com/mobility, last accessed 28 Oct 2020), and U.S. Energy Information Agency electricity consumption (https://www.eia.gov/electricity/data/browser/#/topic/, last accessed 10 Aug 2020).

The CAADA Python package (18) was used to preprocess the PeMS vehicle counts and Strohmeier et al. (2) flight data, as well as download Port of LA and Port of Oakland container moves. For the purposes of Fig. 3, "Bay Area" is defined as Alameda, Contra Costa, Marin, San Mateo, San Francisco, Santa Clara, and Santa Cruz counties, while "LA" is defined as Los Angeles, Orange, Riverside, San Bernardino, Santa Barbara, and Ventura counties. For flight data, shipping data, and traffic data, daily values were normalized such that 15 Jan 2020 is 100% and monthly values were normalized such that Jan 2020 was 100%. For electricity use data, each month's value is the 2020 use as a percentage of 2019 use in the same month.

Dataset	Used for	Link	Last access	Citation
Oxford Stringency Index	Human activity metrics	https://www.bsg.ox.ac.uk/research/research-projects/coronavirus-government-response-tracker	11 Nov 2020	(1)
OpenSky-derived flight data	Human activity metrics	https://zenodo.org/record/3928564	11 Nov 2020	(2)
Port of Oakland container moves	Human activity metrics	https://www.oaklandseaport.com/performance/facts-figures/	11 Nov 2020	
Port of LA container moves	Human activity metrics	https://www.portoflosangeles.org/business/statistics/container-statistics	11 Nov 2020	
Port of Long Beach container moves	Human activity metrics	https://www.polb.com/business/port-statistics/#teus-archive-1995-to-present	10 Nov 2020	
Caltrans PeMS	Human activity & SF emissions	https://pems.dot.ca.gov/	11 Nov 2020	
Apple mobility trends	Human activity metrics	https://covid19.apple.com/mobility	27 Oct 2020	
US EIA electricity use	Human activity metrics	https://www.eia.gov/electricity/data/browser/#/topic/	10 Aug 2020	
CARB air quality data	LA Basin analysis	https://www.arb.ca.gov/aqmis2/aqdselect.php	11 Nov 2020	
OMI NO_2 columns	Global model assimilation (OPE)	http://www.qa4ecv.eu/ecv/no2-pre/data	11 Nov 2020	(3, 4)
TROPOMI NO_2 columns	Global model assimilation (OPE)	http://www.tropomi.eu/data-products/nitrogen-dioxide	11 Nov 2020	(5)
MOPITT CO	Global model assimilation (OPE)	https://www2.acom.ucar.edu/mopitt	11 Nov 2020	(6)
OMI SO_2 columns	Global model assimilation (OPE)	https://disc.gsfc.nasa.gov/datasets/OMSO2_003/summary	11 Nov 2020	(7, 8)
MLS O_3	Global model assimilation (OPE)	https://mls.jpl.nasa.gov/products/o3_product.php	11 Nov 2020	(9, 10)
MLS HNO_3	Global model assimilation (OPE)	https://mls.jpl.nasa.gov/products/hno3_product.php	11 Nov 2020	(9, 11)
BEACO2N CO_2 data	SF CO_2 emissions estimates	https://beacon.berkeley.edu/	11 Nov 2020	
NOAA HRRR meteorology	SF CO_2 emissions estimates	https://rapidrefresh.noaa.gov/hrrr/	11 Nov 2020	

Table S1. Public data sources used in this paper. The "Used for" column gives the part of the analysis in which that data was used.

TROPOMI NO_2 timeseries. For our analysis we re-grid the operational TROPOMI tropospheric vertical column NO_2, with native pixels of approximately 3.5×7 km^2 for 2019 and 3.5×5.5 km^2 for 2020, to a newly defined $0.01^\circ \times 0.01^\circ$ grid (approximately 1×1 km^2) centered over each of the three cities: Los Angeles, Lima, and Shanghai. Before re-gridding, the data are filtered so as to use only the highest quality measurements (quality assurance flag (QA_flag) > 0.75). By restricting to this QA value, we are removing mostly cloudy scenes (cloud radiance fraction > 0.5) and observations over snow-ice. Once the re-gridding has been completed, the data is binned temporally during a 15-day rolling timeframe and spatially over the metropolitan area, which we loosely define as a $1^\circ \times 1^\circ$ box over the city center. The rolling 75th percentile of the binned data during the first five months of 2019 annd 2020 are shown in top row of Figure 4. There is some evidence that the current TROPOMI operational NO_2 product may have a low bias of 20 to 40% in polluted areas; much of this bias may be attributed to the air mass factor (19–21). We limit our analysis to relative trends, which reduces this uncertainty.

LA Basin AQ analysis. The hourly ambient temperature and concentrations of PM2.5, NO_2, and O_3 in the South Coast Air Basin for the period of 1 Jan 2015 to 30 Sept 2020 were downloaded from the California Air Resources Board Air Quality Data Query Tool (https://www.arb.ca.gov/aqmis2/aqdselect.php). It should be noted that the 2020 data are preliminary, unvalidated, and subject to change. The following steps were taken for data analysis:

1. Only the monitoring sites that had complete data between 2015 and 2020 were considered in this analysis. Near-road monitoring sites were not included in the analysis. Figure S8 and Table S2 show the location of the monitoring sites considered in this analysis and the parameters measured at each site, respectively.

2. For every date and site, the 1hr daily maximum (DM) temperature, 24hr average PM2.5, 1hr DM NO_2, and 8hr average DM O_3 were calculated.

3. For every date, the average of the above-mentioned parameters was calculated across all monitoring sites. 7-day moving averages were then calculated and presented by day of year in Figure 4 for 2020 and the average ($\pm$ range) of [2015-2019]. The background colors in Figure 4 illustrate the difference between the 7-day moving average temperature in 2020 and the average ($\pm 1\sigma$) temperature in [2015-2019] by day of year.

4. Using the data in step 2, the percent change in monthly average concentrations of 1hr DM NO_2 and 8hr DM O_3 between 2020 and the average of [2015-2019] was calculated by month and site as shown in Figures S1 and S2.

Global ozone production efficiency calculation. We evaluated the seasonal and regional changes in the global tropospheric ozone response to COVID-19 NO_x emissions using a state-of-the-art chemical data assimilation system. Anthropogenic NO_x emission reductions linked to the COVID-19 pandemic were estimated as the difference between 2020 emissions and climatological (baseline) emissions for 2010-2019 estimated from our decadal chemical reanalysis constrained by multiple satellite measurements. The assimilation system uses the MIROC-CHASER global chemical transport model and an ensemble Kalman filter technique (22). This approach allows us to capture temporal and spatial variations in transport and chemical reactions in the emission and concentration estimates. The results for 2020 were used previously to evaluate the air quality response to Chinese COVID-19 lockdown (23), and show reasonable agreements with the observed concentrations from in-situ, ozonesonde, and satellite ozone measurements globally for 2005-2018 (23) as well as for 2020 (Miyazaki et al., paper in prep.).

In order to evaluate seasonal and regional differences in the ozone response, the ozone production efficiency (OPE) was estimated based on model sensitivity calculations using the 2020 and baseline emissions for February-July 2020. The OPE was calculated using the simulated global tropospheric ozone burden changes corresponding to changing NO_x emissions (i.e., the COVID-19 emission anomaly); the analysis was performed separately for each of the selected megacities. The model simulations were conducted from the beginning to the end of each month for the time period February to June, 2020, using the same initial conditions. The simulated tropospheric ozone burden averaged over the last 5 days of each month was compared between the simulations using the 2020 and baseline emissions. The analysis thus provides information on monthly changes in the ozone response (Tg) to reduced NO_x emissions (Tg per year) for each megacity separately.

PM2.5 simulations. We used the GEOS-Chem (v9-02) model with a bi-directional NH_3 flux scheme (24) at the nested resolution of $0.3125^\circ \times 0.25^\circ$ latitude to explore the sensitivity of inorganic aerosol formation to NO_x emission reductions in Los Angeles (118.239° W, 34.052° N) during COVID-19. Our detailed O_3-NO_x-VOC-aerosol simulations were driven by Goddard Earth Observing System (GEOS-FP 5.22.0) assimilated meteorological fields and include anthropgenic/biogenic/biomass burning emissions (25–27), gas-phase chemistry (28) and inorganic aerosol partitioning (29), wet/dry depositions (30–32) and transport. We first scaled anthropogenic NO_x and SO_2 emissions from HTAP v2 (25) (originally for the year 2010) to the year 2017 using satellite-derived SO_2 and NO_x emission reduction ratios (33) as our base emissions, which refer to emissions before lockdown during COVID-19. We scaled our base anthropogenic NO_x emissions in March by BAU/COVID monthly NO_x emission ratios from Miyazaki et al. (23) as our BAU/COVID emissions. In the COVID-19 simulations, the NO_x emissions started to decrease on March 1st.

We calculated the gas ratio (34) using Eq. (1):

$$\text{gas ratio} = \frac{[NH_3] + [NH_4^+] - 2[SO_4^{2-}]}{[HNO_3] + [NO_3^-]} \quad [1]$$

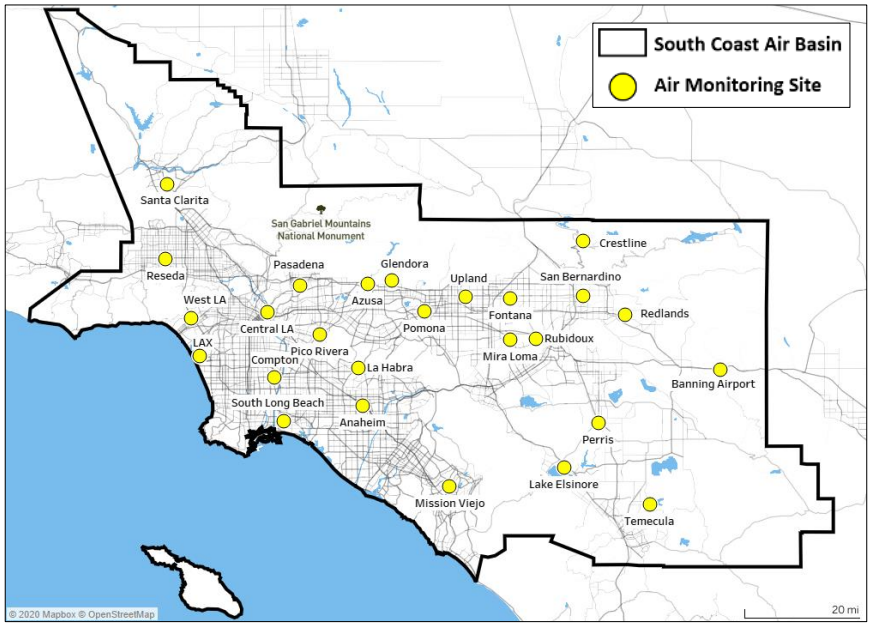

Fig. S8. Location of South Coast Air Basin monitoring sites included in this analysis.

Site	Temperature	O_3	PM2.5	NO_2
Anaheim	✓	✓	✓	✓
Azusa	✓	✓		✓
Banning airport	✓	✓	✓	✓
Central LA	✓	✓	✓	✓
Compton	✓	✓		✓
Crestline	✓	✓	✓	
Fontana	✓	✓		✓
Glendora	✓	✓	✓	✓
La Habra		✓		✓
Lake Elsinore	✓	✓	✓	✓
LAX		✓		✓
Mira Loma	✓	✓	✓	✓
Mission Viejo	✓	✓		
Pasadena		✓		✓
Perris	✓	✓		
Pico Rivera	✓	✓		✓
Pomona		✓		✓
Redlands		✓		
Reseda		✓	✓	✓
Rubidoux	✓	✓	✓	✓
San Bernadino	✓	✓		✓
Santa Clarita	✓	✓	✓	✓
South Long Beach			✓	
Upland	✓	✓	✓	✓
West LA		✓		✓
Temecula	✓	✓	✓	

Table S2. Parameters used from each South Coast Air Basin monitoring site.

$[NH_3]$, $[NH_4^+]$, $[SO_4^{2-}]$, $[HNO_3]$ and $[NO_3^-]$ are in units of molar concentrations (mol m^{-3}) and include both gas-phase and aerosol-phase. This gas ratio is an indicator of NH_4NO_3 production sensitivity to NO_x emission change and NH_3 emission change. Values > 1 indicate that NH_4NO_3 production is NO_x limited; values < 1 indicate it is NH_3 limited.

SF Bay Area CO_2 emissions estimates. To derive top-down emissions, Turner et al. (35) used 12 weeks of observational data from the $BEACO_2N$ network (36) to estimate the most likely CO_2 fluxes from the San Francisco Bay Area before and during the shelter-in-place order (6 weeks of data before and 6 weeks of data during). Specifically, they estimated hourly fluxes at 900-m spatial resolution over the region and solved for posterior fluxes as:

$$\hat{\mathbf{x}} = \mathbf{x_a} + (\mathbf{HB})^T \left(\mathbf{HBH}^T + \mathbf{R}\right)^{-1} (\mathbf{y} - \mathbf{Hx_a}) . \quad [2]$$

$\hat{\mathbf{x}}$ $(m \times 1)$ is the posterior emissions, $\mathbf{x_a}$ $(m \times 1)$ is the prior emissions, $\mathbf{y}$ $(n \times 1)$ is the $BEACO_2N$ observations, $\mathbf{H}$ $(n \times m)$ is the matrix of footprints from HRRR-STILT, $\mathbf{R}$ $(n \times n)$ is the model-data mismatch error covariance matrix, and $\mathbf{B}$ $(m \times m)$ is the prior error covariance matrix.

Turner et al. (35) used meteorological fields from the NOAA High Resolution Rapid Refresh (HRRR), to drive the Stochastic Time-Inverted Lagrangian Transport (STILT) model, a Lagrangian particle dispersion model. Those trajectories were then used to construct measurement footprints ($\mathbf{H}$), representing the sensitivity of the measurement to a perturbation in emissions from a given location. Their prior emissions were adapted from previous work (37) with a biosphere derived from TROPOMI SIF observations (38). Upwind concentrations were taken from NOAA observations in the Pacific or AmeriFlux observations in California, depending on the endpoint of the back trajectory.

To derive bottom-up emissions, total hourly vehicle flow and percentage of trucks were retrieved from http://pems.dot.ca.gov from approximately 1800 traffic counting stations hosted by the Caltrans Performance Measurement System (PeMS) for January to June in 2019 and 2020. These sites encompass all highway sites within the 2020 footprint of the Berkeley Air Quality and CO_2 Network ($BEACO_2N$), as described in Turner et al. (35). These stations count vehicle flow using magnetic loops imbedded in roadways and estimate truck fraction using calculated vehicle speed and assumptions about vehicle length (39). For hours during which fewer than 50% of measurements were reported, we fill in total vehicle flow gaps by using linear fits to nearest neighbor sites and gaps in truck flow using hour-of-day-specific linear fits between neighboring sites. We calculate both car and truck vehicle miles traveled (VMT) for each highway segment during each hour using segment lengths obtained from the PeMS database. VMT for highway segments within the BEACO2N footprint are summed to obtain regional highway truck and car VMT for every hour. VMT is then converted to CO_2 using fleet estimates for fuel efficiency.

US CO_2 emissions estimates. Fuel consumption data from the U.S. Energy Information Administration (EIA) is used to generate weekly (Sat-Fri) estimates of $FFCO_2$ emissions between January 2005 and the week ending September 18, 2020. The input data includes all petroleum fuel consumption by fuel type, natural gas consumption by sector, and coal consumption by sector. These are organized into six fossil fuel consumption sectors: 1) gasoline-fueled transportation; 2) commercial surface transportation (i.e. land and water); 3) aviation; 4) electricity generation; 5) industrial energy consumption; and 6) residential/commercial energy consumption. Standard CO_2 emission factors are applied to the individual fuel types to achieve $FFCO_2$ emissions (40). To facilitate comparison to emission values in 2020, all time-series of $FFCO_2$ emissions are detrended. Comparison of weekly $FFCO_2$ emissions in 2020 are made to the long-term (2005 to 2019) weekly detrended median values and their associated 15-member ensemble distribution. Statistical significance is defined by departures that exceed a) the 1st/3rd quartile of the weekly ensemble distributions from 2005-2019, referred to as "partly significant" and b) the maximum/minimum distributions of the same weekly ensembles, referred to as "significant". The latter criteria are considered akin to a 2-sigma boundary for Gaussian statistics.

Global CO_2 growth rate simulations. The Goddard Earth Observing System (GEOS) is a flexible modeling and data assimilation system that has been widely used to study atmospheric composition and the carbon cycle (41). It includes the capability to simulate CO_2 concentrations in near real time by extrapolating previous year's biosphere and ocean fluxes (42). Here, we also include tracers that separately quantify the atmospheric impact of daily differences in fossil emissions between 2020 and 2019 using country-level estimates from Liu et al. (14) that are spatially disaggregated to ∼10-km using information from the Emissions Database for Global Atmospheric Research (43).

Global CO_2 emissions estimates. We calculated the daily global fossil CO_2 emissions in 2020 (updated to August 31st), as well as the daily sectoral emissions from power sector, industry sector, transport sector (including ground transport, aviation and shipping), and residential sector respectively. The estimates are based on a set of near real time dataset including hourly to daily electrical power generation data from national electricity operation systems of 31 countries, real-time mobility data (TomTom city congestion index data of 416 cities worldwide and FlightRadar24 individual flight location data), monthly industrial production data (calculated separately by cement production, steel production, chemical production and other industrial production of 27 industries) or indices (primarily Industrial Production Index) from national statistics of 62 countries/regions, and monthly fuel consumption data corrected for the daily population-weighted air temperature in 206 countries.

References

1. Hale T, et al. (2020) Oxford COVID-19 government response tracker. Blavatnik School of Government.

2. Strohmeier M, Olive X, Lübbe J, Schäfer M, Lenders V (2020) Crowdsourced air traffic data from the OpenSky network 2019–20. *Earth System Science Data Discussions* 2020:1–15.
3. Boersma KF, et al. (2017) QA4ECV NO_2 tropospheric and stratospheric column data from OMI. doi: 10.21944/QA4ECV-NO2-OMI-V1.1.
4. Boersma KF, et al. (2018) Improving algorithms and uncertainty estimates for satellite NO_2 retrievals: results from the quality assurance for the essential climate variables (QA4ECV) project. *Atmospheric Measurement Techniques* 11(12):6651–6678.
5. van Geffen J, et al. (2020) S5P TROPOMI NO_2 slant column retrieval: method, stability, uncertainties and comparisons with OMI. *Atmospheric Measurement Techniques* 13(3):1315–1335.
6. Deeter MN, et al. (2017) A climate-scale satellite record for carbon monoxide: the MOPITT Version 7 product. *Atmospheric Measurement Techniques* 10(7):2533–2555.
7. Krotkov NA, et al. (2016) Aura OMI observations of regional SO_2 pollution changes from 2005 to 2015. *Atmospheric Chemistry and Physics* 16(7):4605–4629.
8. Can Li, Nickolay A. Krotkov PL, Joiner J (2020) OMI/Aura Sulphur Dioxide (SO_2) Total Column 1-orbit L2 Swath 13x24 km V003, Greenbelt, MD, USA, Goddard Earth Sciences Data and Information Services Center (GES DISC). Accessed: 11 Nov 2020, doi: 10.5067/Aura/OMI/DATA2022.
9. Livesey NJ, et al. (2018) Earth Observing System (EOS) Aura Microwave Limb Sounder (MLS) Version 4.2x Level 2 and 3 data quality and description document (JPL D-33509 Rev. E). Available from, https://mls.jpl.nasa.gov/data/v4-2_data_quality_document.pdf, last access: 21 Nov 2020.
10. Schwartz M, Froidevaux L, Livesey N, Read W (2015) MLS/Aura Level 2 Ozone (O_3) Mixing Ratio V004, Greenbelt, MD, USA, Goddard Earth Sciences Data and Information Services Center (GES DISC). doi: 10.5067/Aura/MLS/DATA2017.
11. Manney G, Santee M, Froidevaux L, Livesey N, Read W (2015) MLS/Aura Level 2 Nitric Acid (HNO_3) Mixing Ratio V004, Greenbelt, MD, USA, Goddard Earth Sciences Data and Information Services Center (GES DISC). doi: 10.5067/Aura/MLS/DATA2012.
12. Friedlingstein P, et al. (2019) Global carbon budget 2019. *Earth System Science Data* 11(4):1783–1838.
13. Le Quéré C, et al. (2020) Temporary reduction in daily global CO_2 emissions during the COVID-19 forced confinement. *Nature Climate Change* 10(7):647–653.
14. Liu Z, et al. (2020) Near-real-time monitoring of global CO_2 emissions reveals the effects of the COVID-19 pandemic. *Nature Communications* 11(1).
15. Saunois M, et al. (2020) The global methane budget 2000–2017. *Earth System Science Data* 12(3):1561–1623.
16. Schäfer M, Strohmeier M, Lenders V, Martinovic I, Wilhelm M (2014) Bringing Up OpenSky: A Large-scale ADS-B Sensor Network for Research. *Proceedings of the 13th IEEE/ACM International Symposium on Information Processing in Sensor Networks (IPSN)* pp. 83–94.
17. Olive X (2019) traffic, a toolbox for processing and analysing air traffic data. *Journal of Open Source Software* 4(39).
18. Laughner J (2020) COVID Atmospheric Ancillary Data Agglomerator, v0.1.0.
19. Griffin D, et al. (2019) High-resolution mapping of nitrogen dioxide with TROPOMI: First results and validation over the Canadian oil sands. *Geophysical Research Letters* 46(2):1049–1060.
20. Judd LM, et al. (2020) Evaluating Sentinel-5P TROPOMI tropospheric NO_2 column densities with airborne and Pandora spectrometers near New York City and Long Island Sound. *Atmospheric Measurement Techniques* 13(11):6113–6140.
21. Verhoelst T, et al. (2020) Ground-based validation of the copernicus Sentinel-5p TROPOMI NO_2 measurements with the NDACC ZSL-DOAS, MAX-DOAS and Pandonia global networks. *Atmospheric Measurement Techniques Discussions* 2020:1–40.
22. Miyazaki K, et al. (2020) Updated tropospheric chemistry reanalysis and emission estimates, TCR-2, for 2005–2018. *Earth System Science Data* 12(3):2223–2259.
23. Miyazaki K, et al. (2020) Air quality response in China linked to the 2019 novel coronavirus (COVID-19) lockdown. *Geophysical Research Letters* 47(19):e2020GL089252. doi: 10.1029/2020GL089252.
24. Zhu L, et al. (2015) Global evaluation of ammonia bidirectional exchange and livestock diurnal variation schemes. *Atmospheric Chemistry and Physics* 15(22):12823–12843.
25. Janssens-Maenhout G, et al. (2015) HTAP_v2.2: a mosaic of regional and global emission grid maps for 2008 and 2010 to study hemispheric transport of air pollution. *Atmospheric Chemistry and Physics* 15(19):11411–11432.
26. Guenther AB, et al. (2012) The model of emissions of gases and aerosols from nature version 2.1 (MEGAN2.1): an extended and updated framework for modeling biogenic emissions. *Geoscientific Model Development* 5(6):1471–1492.
27. van der Werf GR, et al. (2010) Global fire emissions and the contribution of deforestation, savanna, forest, agricultural, and peat fires (1997–2009). *Atmospheric Chemistry and Physics* 10(23):11707–11735.
28. Mao J, et al. (2010) Chemistry of hydrogen oxide radicals (HO_x) in the arctic troposphere in spring. *Atmospheric Chemistry and Physics* 10(13):5823–5838.
29. Park RJ (2004) Natural and transboundary pollution influences on sulfate-nitrate-ammonium aerosols in the United States: Implications for policy. *Journal of Geophysical Research* 109(D15).
30. Liu H, Jacob DJ, Bey I, Yantosca RM (2001) Constraints from ^{210}Pb and ^{7}Be on wet deposition and transport in a global three-dimensional chemical tracer model driven by assimilated meteorological fields. *Journal of Geophysical Research: Atmospheres* 106(D11):12109–12128.

31. Wang Q, et al. (2011) Sources of carbonaceous aerosols and deposited black carbon in the arctic in winter-spring: implications for radiative forcing. *Atmospheric Chemistry and Physics* 11(23):12453–12473.
32. Amos HM, et al. (2012) Gas-particle partitioning of atmospheric Hg(II) and its effect on global mercury deposition. *Atmospheric Chemistry and Physics* 12(1):591–603.
33. Miyazaki K, et al. (2019) Chemical reanalysis products, doi: 10.25966/9qgv-fe81.
34. Ansari AS, Pandis SN (1998) Response of inorganic PM to precursor concentrations. *Environmental Science & Technology* 32(18):2706–2714.
35. Turner AJ, et al. (2020) Observed impacts of COVID-19 on urban CO_2 emissions. *Geophysical Research Letters* 47(22):e2020GL090037.
36. Shusterman AA, et al. (2016) The BErkeley atmospheric CO_2 observation network: initial evaluation. *Atmospheric Chemistry and Physics* 16(21):13449–13463.
37. Turner AJ, et al. (2016) Network design for quantifying urban CO_2: assessing trade-offs between precision and network density. *Atmospheric Chemistry and Physics* 16(21):13465–13475.
38. Turner AJ, et al. (2020) A double peak in the seasonality of California's photosynthesis as observed from space. *Biogeosciences* 17(2):405–422.
39. Kwon J, Varaiya P, Skabardonis A (2003) Estimation of truck traffic volume from single loop detectors with lane-to-lane speed correlation. *Transportation Research Record* 1856(1):106–117.
40. Gurney KR, et al. (2020) The Vulcan version 3.0 high-resolution fossil fuel CO_2 emissions for the United States. *Journal of Geophysical Research: Atmospheres* 125(19).
41. Ott LE, et al. (2015) Assessing the magnitude of CO_2 flux uncertainty in atmospheric CO_2 records using products from NASA's Carbon Monitoring Flux Pilot Project. *Journal of Geophysical Research: Atmospheres* 120(2):734–765.
42. Weir B, et al. (2020) Calibrating satellite-derived carbon fluxes for retrospective and near real-time assimilation systems.
43. Crippa M, et al. (2020) High resolution temporal profiles in the emissions database for global atmospheric research. *Scientific Data* 7(1).